Experimental Aeroelastic Behavior of Forward-Swept Graphite/Epoxy Wings with Rigid-Body Freedom

Gun-Shing Chen* and John Dugundji†
Massachusetts Institute of Technology, Cambridge, Massachusetts

An analytical and experimental investigation was made of the aeroelastic flutter and divergence behavior of graphite/epoxy forward-swept wings with rigid-body pitch and plunge freedoms present. A complete, two-sided, 30 deg forward-swept wing aircraft model was constructed and mounted with low-friction bearings in a low-speed wind tunnel. Four different ply layup wings could be interchanged on the model, namely, $[0_2/90]_s$, $[15_2/0]_s$, $[30_2/0]_s$, and $[-15_2/0]_s$. Wind-tunnel tests on the "free"-flying models revealed body freedom flutter, bending-torsion flutter, and a support dynamic instability that could be eliminated by proper adjustment of the support stiffness. Good agreement with linear theory was found for all the observed instabilities. Additional tests on the models with rigid-body pitch only gave lower critical speeds, while tests on the cantilever wings gave higher speeds. The $[15_2/0]_s$ wing gave the best tailored aeroelastic behavior.

Introduction

RENEWED interest in forward-swept wing configurations has lately inspired many studies concerning the aeroelastic behavior, aeroelastic tailoring, and active control technology for such wings. See Shirk et al.[1] for a recent comprehensive survey of the subject. The early studies of forward-swept wing aeroelasticity concerned themselves mostly with the flutter and divergence of cantilever restrained wings. See, for example, Refs. 2–5. Recently, however, several authors[6–9] pointed out the significant effects of rigid-body motions in modifying the cantilever aeroelastic behavior. Since the bending frequency of a forward-swept wing is lowered due to the approach to wing divergence, a new low-frequency "body freedom flutter" coupling wing bending with the aircraft rigid-body pitch and plunge motions becomes possible in free flight. This effect was explored on a limited basis in Ref. 6 by a simple half-plane model without a canard and rigid-body plunge motion present and gave some initial trends. Further work on a large, half-plane aircraft model was done at NASA Langley and is reported on in Ref. 10. Generally, however, the experimental data on this effect for forward-swept wing aircraft are limited.

In previous investigations at MIT, the aeroelastic behavior of unswept and forward-swept graphite/epoxy cantilever wings was studied experimentally.[11,12] The present paper extends these investigations to include the effect of rigid-body freedoms on the aeroelastic behavior. A generic, full-span, 30 deg forward-swept wing aircraft model was constructed and mounted with low-friction support bearings in MIT's low-speed tunnel (Fig. 1), using nominally the same wings as in previous cantilever tests. The model was statically stable with a measured static margin of 18%. The effects of aeroelastic tailoring in "free" flight were explored by four different wing layups, namely, $[0_2/90]_s$, $[15_2/0]_s$, $[30_2/0]_s$, and $[-15_2/0]_s$.

Received April 1, 1986; presented as Paper 86-0971 at the AIAA/ASME/ASCE/AHS 27th Structures, Structural Dynamics, and Materials Conference, San Antonio, TX, May 19–21, 1986; revision received Jan. 5, 1987.

*Research Assistant, Technology Laboratory for Advanced Composites, Department of Aeronautics and Astronautics. Member AIAA.

†Professor, Department of Aeronautics and Astronautics. Member AIAA.

Analysis

The flutter analysis of an aircraft in steady flight is formulated by the Rayleigh-Ritz approximation. The development of the mathematical model governing the pure longitudinal motions considers small disturbances from a steady rectilinear flight. The small disturbances include the vehicle rigid-body motions and elastic deformations and are described in an axis system moving steadily with the vehicle in the still air. For steady level flight, these axes can be considered fixed in space while the air is flowing oppositely at constant speed and are identical to the tunnel support axes as shown in Fig. 2.

The analysis hypothesizes an aircraft with flexible wing, rigid fuselage, and canard surface. Any vertical displacement of the aircraft with respect to a space-fixed horizontal plane is approximated by a superposition of the assumed modes, i.e.,

$$w(x,y,t) = \sum_{i=1}^{7} \gamma_i(x,y) q_i(t) = \sum_{i=1}^{7} \phi_i(x) \psi_i(y) q_i(t) \tag{1}$$

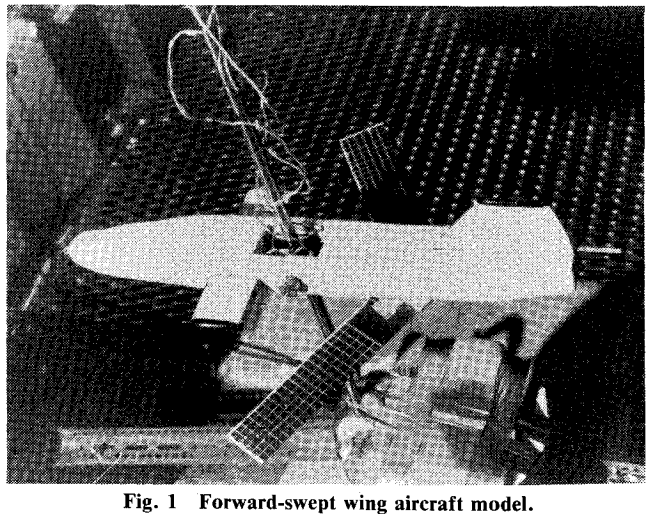

Fig. 1 Forward-swept wing aircraft model.

The assumed modes $\gamma_i(x,y)$ include vertical translation or plunging, pitching displacement about the aircraft center of gravity and five elastic modes. These elastic modes represent wing deformations relative to the wing root position for the rigid-fuselage assumption. Using the same elastic modes given in Ref. 12, the seven assumed modes are

$\phi_1(x) = 1$

$\phi_2(x) = 1$

$\phi_3(\bar{x}) =$ first cantilever beam bending mode

$\phi_4(\bar{x}) =$ second cantilever beam bending mode

$\phi_5(\bar{x}) = \sin(\pi\bar{x}/2\bar{\ell})$

$\phi_6(\bar{x}) = \sin(3\pi\bar{x}2\bar{\ell})$

$\phi_7(\bar{x}) = \bar{x}/\bar{\ell}\,(1-\bar{x}/\bar{\ell})$

$\psi_1(y) = 1$

$\psi_2(y) = y$

$\psi_3(\bar{y}) = 1$

$\psi_4(\bar{y}) = 1$

$\psi_5(\bar{y}) = \bar{y}/\bar{c}$

$\psi_6(\bar{y}) = \bar{y}/\bar{c}$

$\psi_7(\bar{y}) = [4(\bar{y}/\bar{c})^2 - \frac{1}{3}]$

Following as in Ref. 12 for these modes, the kinetic energy T for the aircraft is

$$T = \frac{1}{2}\int_{A/C} m\dot{w}^2 \,\mathrm{d}x\mathrm{d}y \tag{2}$$

where $\dot{(\ )} = \mu/\mu t$ and m is the mass per area in the $x-y$ plane. The total potential energy for the aircraft contains only the strain energy of the elastic wing, i.e.,

$$U = \frac{1}{2}\int_{\text{wing}} [D_{11}w^2_{,\bar{x}\bar{x}} + 2D_{12}w_{,\bar{x}\bar{x}}w_{,\bar{y}\bar{y}} + D_{22}w^2_{,\bar{y}\bar{y}} + 4D_{16}w_{,\bar{x}\bar{x}}w_{,\bar{x}\bar{y}} + 4D_{26}w_{,\bar{y}\bar{y}}w_{,\bar{x}\bar{y}} + 4D_{66}w^2_{,\bar{x}\bar{y}}]\,\mathrm{d}\bar{x}\mathrm{d}\bar{y} \tag{3}$$

where $w_{,x}$ denotes $\partial w/\partial x$ and so on and the D_{ij} are laminate bending stiffness terms for the wings from classical laminate plate theory. In analyzing the tunnel-supported configuration, the additional potential energy terms given by the support mechanical springs are

$$U = \tfrac{1}{2}K_z q_1^2 + \tfrac{1}{2}K_\Theta q_2^2 \tag{4}$$

where K_z and K_Θ are the support plunge and pitch spring rates. Placing the kinetic and potential energy terms into Lagrange's equations results in a set of ordinary differential equations of motion

$$M\{\ddot{q}\} + K\{q\} = \{Q\} \tag{5}$$

where M and K are generalized inertia and stiffness matrices and $\{q\} = [q_1, q_2, q_3, q_4, q_5, q_6, q_7]^T$. The generalized force $\{Q\}$ is derived from the expression of the virtual work

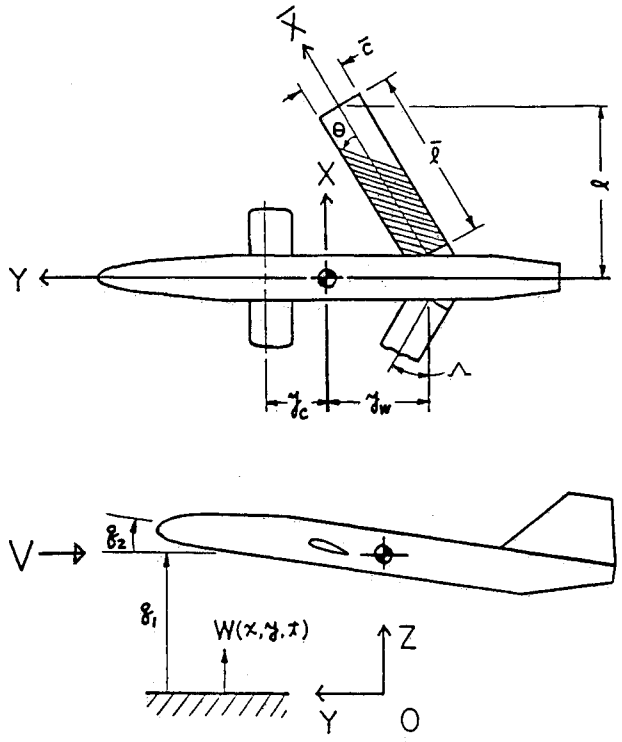

Fig. 2 Mathematical model and axis system.

δW_e as

$$\delta W_e = \int_{A/C} \Delta p\, \delta w \,\mathrm{d}x\mathrm{d}y$$

$$= L_{\text{body}}\delta q_1 + M_{\text{body}}\delta q_2 + \int_{\text{wing}} \Delta p\, \delta w \,\mathrm{d}x\mathrm{d}y \tag{6}$$

where "body" denotes contributions from the canard/fuselage combination. Using the airloads described by two-dimensional streamwise-strip theory, the virtual work expression is then

$$\delta W_e = L_{\text{body}}\delta q_1 + M_{\text{body}}\delta q_2 + \int_{\text{wing}} (L\delta h + M\delta\alpha + N\delta\xi)\mathrm{d}x$$

$$= \sum_{i=1}^{7} Q_i \delta q_i \tag{7}$$

where the sectional deformations across the wing are defined and expressed in terms of the assumed modes q_i as

$$h = q_1 + (y_w - \bar{x}\sin\Lambda)q_2 + \phi_3 q_3 + \phi_4 q_4$$

$$\alpha = q_2 - (\phi_{3,\bar{x}}q_3 + \phi_{4,\bar{x}}q_4)\sin\Lambda + 1/\bar{c}(\phi_5 q_5 + \phi_6 q_6)\cos\Lambda$$

$$\xi = \phi_7 q_7 \tag{8}$$

Since the streamwise section is not normal to the structural span of a swept wing, the sectional twist and camber change are approximated by the assumed modes in Eq. (8). In here, Λ and y_w would both be negative values for a forward-swept wing aircraft.

Because of the inherent aeroelastic destiffening of the forward-swept wing and the aerodynamic stiffening of the short period mode, the interaction between the elastic and

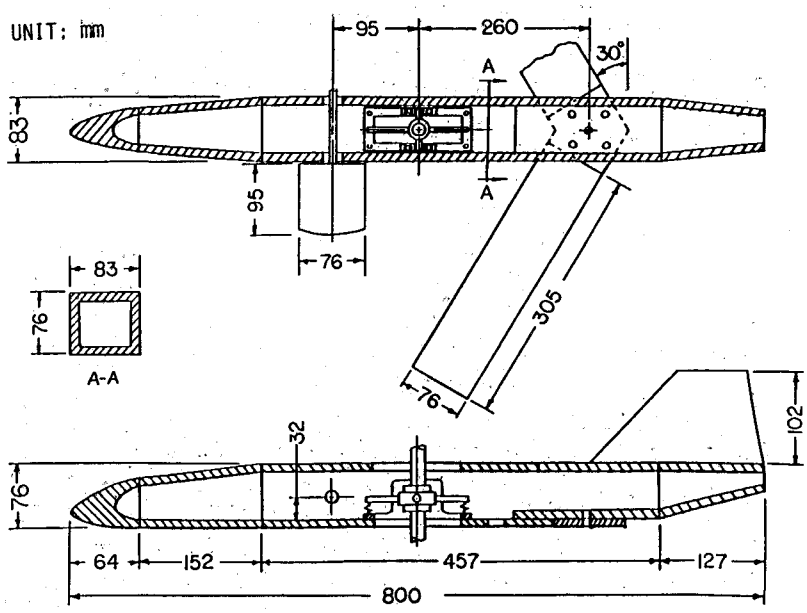

Fig. 3 Aircraft model layout.

rigid-body modes is of great interest. To describe the stiffness and damping characteristics of these modes as airspeed increases, airloads due to the arbitrary transient wing motions are convenient. For the present study, two-dimensional incompressible strip theory airloads were used and the Theodorsen function was approximated in the Laplace domain by the rational polynomial

$$C(\bar{p}) = (a\bar{p}+\beta)/(\bar{p}+\beta) \tag{9}$$

where $a=0.55$, $\beta=0.15$, $\bar{p}$ is the dimensionless Laplace variable $\bar{p}=pb/U$, and $p=\sigma+i\omega$. This simple function gave a reasonable fit to the Theodorsen function over reduced frequencies $k=b\omega/U$ from 0 to 1. The transient airloads could then be described in the Laplace domain as

$$\begin{aligned}\hat{L}(\bar{p}) &= 2\pi\rho U^2 b\cos\Lambda \\ &\{[B_{2A}\bar{p}^2+B_{1A}\bar{p}+B_{OA}+G_{1A}\bar{p}/(\bar{p}+\beta)]\hat{h}/b \\ &+[B_{2B}\bar{p}^2+B_{1B}\bar{p}+B_{OB}+G_{1B}\bar{p}/(\bar{p}+\beta)]\hat{\alpha} \\ &+[B_{2C}\bar{p}^2+B_{1C}\bar{p}+B_{OC}+G_{1C}\bar{p}/(\bar{p}+\beta)]\hat{\xi}/b\} \\ \hat{M}(\bar{p}) &= \text{etc.} \\ \hat{N}(\bar{p}) &= \text{etc.}\end{aligned} \tag{10}$$

In Eqs. (10), the B_{2A}, B_{1A}, B_{OA}, and G_{1A} coefficients represent the aerodynamic mass, damping, stiffness, and lag terms, respectively. Placing Eqs. (10) into Eq. (7), introducing h, α, and ξ from Eqs. (8), and defining seven new augmented state variables y_i such that

$$\hat{y}_i(\bar{p}) = \bar{p}/(\bar{p}+\beta)\hat{q}_i(\bar{p}), \quad i=1\text{-}7 \tag{11}$$

allows one to write the generalized aerodynamic forces in transient form as

$$Q_i = \sum_{j=1}^{7}(Q_{ij}^A\ddot{q}_j + Q_{ij}^B\dot{q}_j + Q_{ij}^C q_j + Q_{ij}^D y_j) \tag{12}$$

$$\dot{y}_i + \beta U/b\, y_i = \dot{q}_i, \qquad i=1\text{-}7 \tag{13}$$

where the Q_{ij} are the aerodynamic matrices derived from the virtual work expression. These augmented states increase the order of the system, but allow the convenience of the linear eigenvalue analysis of the constant-coefficient ordinary differential equations. The differential equations representing the aerodynamic lags are incorporated into the aeroelastic equation of motions as

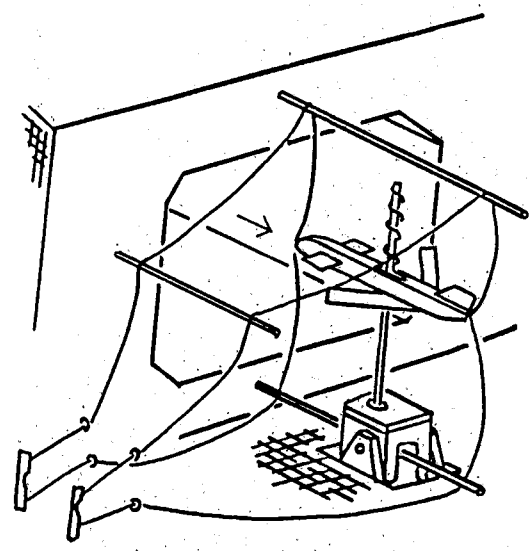

Fig. 4 MIT acoustic wind-tunnel setup.

$$\begin{bmatrix} I & 0 & 0 \\ 0 & (M-Q^A) & 0 \\ 0 & 0 & I \end{bmatrix} \begin{Bmatrix} \dot{q} \\ \ddot{q} \\ \dot{y} \end{Bmatrix} = \begin{bmatrix} 0 & I & 0 \\ (Q^C-K) & (Q^B-C) & Q^D \\ 0 & I & -H \end{bmatrix} \begin{Bmatrix} q \\ \dot{q} \\ y \end{Bmatrix} \tag{14}$$

where I is the identity matrix and H is $\beta U/b\, I$. This yields a set of 21 first-order differential equations. For given values of dynamic pressure, the transient behavior and stability characteristics are determined by setting $q=qe^{pt}$ and $y=ye^{pt}$ and find-

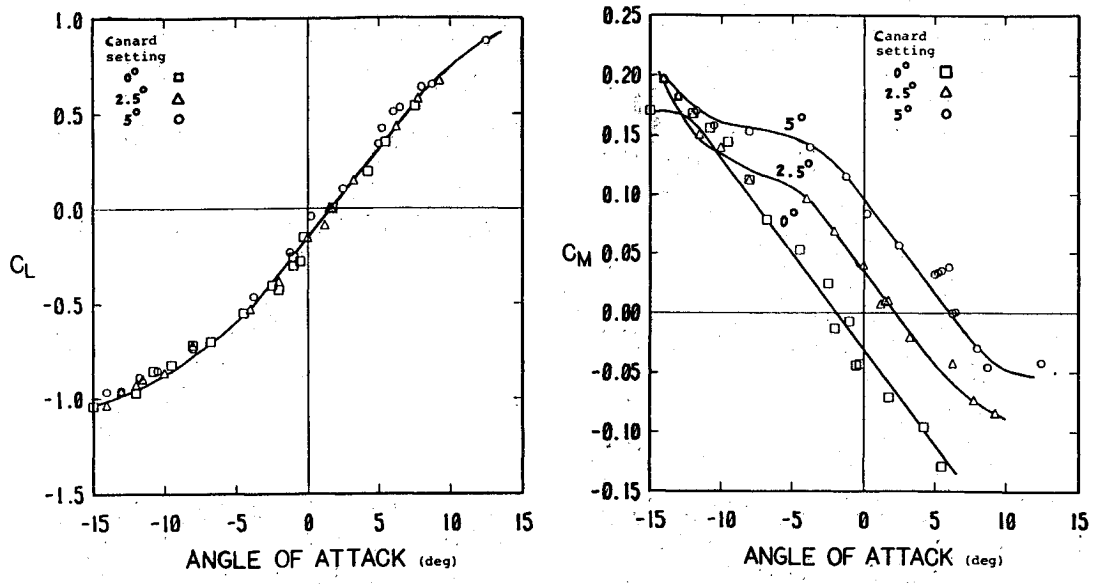

Fig. 5 Aerodynamic coefficients for aircraft model.

ing the eigenvalues p in Eq. (14). The flutter and divergence boundaries are determined by solving the successive eigenvalue problems. The transient aeroelastic behavior is represented by the associated eigenvectors. If the assumed elastic modes are equal to zero, the above stability analysis reduces identically to the rigid aircraft dynamic stability analysis in the space-fixed axis system.

It should be noted that, while unsteady airloads are desired for the wing transient behavior, quasisteady lift and moment expressions associated with the overall aircraft rigid body motions are also used. The canard/wing/fuselage interaction is accounted for by using the empirical aerodynamic derivatives $C_{L\alpha}$, $C_{M\alpha}$, and $C_{M\dot{\alpha}}$, in the total lift and moment expressions

$$L = qS_w C_{L_\alpha} q_2 - qS_w C_{L_\alpha} \dot{q}_1/U - qS_w cC_{M_\alpha} \dot{q}_2/U$$

$$M = qS_w cC_{M_\alpha} \alpha_2 - qS_w cC_{M_\alpha} \dot{q}_1/U + qS_w c^2 C_{M_{\dot{\alpha}}} \dot{q}_2/U \quad (15)$$

where q is the dynamic pressure, S_w the total wing area, and c the mean aerodynamic chord length.

Also, it is to be noted that, since modern control theory is well developed for systems described by finite-order, constant-coefficient ordinary differential equations, the other motivation for using transient airload expressions is the potential of active control design interaction with the aeroelastic analysis.

Experiment

Wind-Tunnel Model, Support System, and Instrumentation

For the purposes of this investigation, a generic, full-span, forward-swept wing aircraft model was constructed. Figure 3 shows the layout of the aircraft model. The principal components are 1) the interchangeable, 30 deg forward-swept, graphite/epoxy flat-plate wings, 2) a sturdy fuselage of balsa wood, and 3) a rigid, all-moving canard surface.

The wing planform was chosen to be the same as those in Refs. 11 and 12, such that the present study complemented the previous cantilever wing studies and isolated the effect of rigid-body freedoms. Instead of using semispan wing models as in Refs. 11 and 12, full-span wing models were fabricated by bonding two 305×76 mm (12×3 in.) laminate plates onto the fiberglass center plate in the 30 deg forward-swept configuration. The laminate plate wings were made up of Hercules AS4/3501-6 graphite/epoxy materials. The effects of the aeroelastic tailoring were demonstrated by a set of four wings with bending/twisting coupling in both favorable and adverse fashions, namely, $[0_2/90]_s$, $[15_2/0]_s$, $[30_2/0]_s$, and $[-15_2/0]_s$ layups. These specimens span the bending/twisting coupling stiffness ratio $D_{16}/\sqrt{D_{11}D_{66}}$ from -0.68 to 0.80.

Table 1 Aircraft model and support properties

Mass	0.956kg
Pitch inertia	0.0178 kg·m^2
Wing mass	0.054kg
Wing span	0.612 m
Wing swept angle	−30 deg
Wing area	0.0538 m^2
Wing aspect ratio	7
Canard area	0.0126 m^2
Fuselage length	0.8 m
Model plunge frequency	0.63 Hz
Model pitch frequency (support 1)	0.20 Hz
Model pitch frequency (support 2)	0.85 Hz

The wind-tunnel investigation of the body freedom flutter requires that the dynamic behavior of a freely flying model be simulated. In the wind-tunnel study, however, the model generally must be somehow restrained and the behavior may be altered to a certain degree by the support system. Without careful consideration of the dynamics of the overall system, an inherent support instability may exist. Various model support systems were studied for the MIT low-speed acoustic wind tunnel, which has a 1.5×2.3 m (5×7.5 ft) freejet test section. The general requirements were to have a soft, stable, and simple model support system with negligible moving mass and low aerodynamic interference, which was well below the predicted body freedom flutter frequency of 2–3 Hz. Because of the model weight, the preselected wing planform was not able to fly the model completely. This overweight factor, together with the requirement of soft support, led to the selection of a vertical rod support system. The vertical rod support system was initially developed by the Boeing Airplane Company and has been successfully used in low-speed wind-tunnel tests.[13] The modified support system for the MIT acoustic wind tunnel included 1) a 1.83 m (6 ft) long, vertically installed, case-hardened steel rod with a 19 mm (¾ in.) diameter, 2) a Thomson super-12 linear bearing sliding on the rod and attached to the fuselage through a pitch bearing mount located at the model center of gravity, 3) a soft helical spring attached to the linear bearing that suspended the model from the top of the vertical rod,

4) a pair of linear springs attached to the pitch gimbals at forward and aft extended arms that provided the support pitching stiffness, and 5) snubber cables attached to the fuselage at the nose and tail locations that lead outside the test section to control sticks. With this test setup, the model was softly restrained in the plunge, pitch, and yaw motions, but totally restrained in the roll, lateral, and fore-and-aft motions except for some slight free play between the linear bearing and rod. Figure 4 shows the layout of the wind-tunnel setup. Details of the model properties and support characteristics are given in Table 1.

Varied instrumentation was used to determine the aeroelastic behavior, including the model rigid-body motions and wing elastic deformation. The wing root bending and torsional strain gages on both sides of the wings monitored the wing motions. A low-friction, conductive film-type potentiometer, flexibly connected to the pitching axle and firmly mounted on the outside of the fuselage, monitored the model's pitch motion. A 203 mm (8 in.) long, 0.51 mm (0.020 in.) thick, cantilever steel beam with a root strain gage was mounted near the top end of the suspension spring to record the model's plunge motion. The wing gage signals were monitored on an oscilloscope. A four-channel strip chart recorder recorded the pitch and plunge signals and the selected side of the wing root bending and torsional gage signals. The left-side wing, facing the tunnel control station, was usually recorded, while the right-side wing was occasionally recorded for comparison purposes. During the tests, video movies of the model responses were also taken for future replay and demonstration.

Aerodynamic Tests

The model center of gravity was located slightly below the pitching axle such that a stable pendulum mode was obtained. To maintain a common reference angle within a test and among other tests, an on-site model balancing was developed as a standard pretesting procedure. With the wind off, the model was balanced in the horizontal position, defined by a level and a tail position scale, by placing balance weights atop the fuselage. After the model was balanced, the pendulum stiffness was measured by placing incremental counterbalancing weights at positions 6 in. in front of and behind the pitching axle and reading the corresponding pitch angles. From the counterbalancing moment vs pitch angle plot, the pendulum stiffness was found.

The aerodynamic characteristics of the "rigid" model were obtained on the actual model at 5 m/s to avoid aeroelastic effects. For the $[0_2/90]_s$ wing, this testing speed was only 6% of the wing divergence dynamic pressure. The procedure of placing counterbalancing weights and reading pitch angles was similar to that of the pendulum stiffness measurement except that the tunnel was now running at a low speed. At each pitch angle, the pure aerodynamic moment was calculated by subtracting the corresponding pendulum moment from the counterbalancing moment. Also, the net lift was calculated by subtracting the counterbalancing weights from the corresponding spring forces. The lift and moment coefficients were then plotted against the pitch angle. This procedure was repeated for several canard settings to determine the proper range of canard setting for flight trimming. The typical canard settings tested were 0, ± 2.5, and ± 5 deg.

Cantilever Wing Flutter Tests

The cantilever wing configuration was set up by blocking the model's plunging freedom with top and bottom stops and varying the wing root angle of attack, i.e., the model pitch angle, with the help of the snubber cables. The testing procedure explored the linear and nonlinear flutter and divergence boundaries. The testing variables were wind-tunnel speed and wing root angle of attack (0–15 deg). At each incremental speed setting, the flutter point was determined by gradually increasing the wing root angle of attack in both the positive and negative sense until flutter was encountered. This procedure was repeated until the flutter or divergence condition could not be suppressed for any setting of the wing root angle of attack. In other words, the positive sense of the critical angle of attack coincided with the negative one.

Body Freedom Flutter Tests

The testing procedure explored the body freedom flutter boundary of the "free"-flying model. The tunnel speed was the only primary variable. A secondary variable was the pitch angle of the trimmed steady flight controlled by the canard setting. Canard settings were chosen to make the trimmed pitch angle slightly positive, i.e., about 2 deg, since models flown at this angle had the most linear moment characteristics and a positive lift to raise the model into the middle of the test section. For the given canard setting, the flutter point was determined by increasing the tunnel speed until body freedom flutter was encountered. At each incremental speed step, subcritical measurements, namely the frequency and critical damping ratio, were made. The pitch and plunge motions were excited by external "kicks" at the tail and near the center of gravity locations. The wing elastic responses were also excited at the wing tip location. The external "kick" was accomplished by using a long wooden stick reaching the model from downstream. In general, this technique was easy and effective, but it became more difficult and dangerous as the tunnel speed was increased. The danger arose from the large increment in the aerodynamic forces resulting from a minor pitch angle increment at high dynamic pressures. The model tended to fly instantly beyond the traveling limits. Without an active compensation scheme in addition to the manual snubber cables, the consequence could be catastrophic. As a result, the subcritical measurements were skipped at high speed.

For comparison purposes, the body freedom flutter of the model free in pitch only was also tested. The pitch-only configuration was set up by blocking the model plunging freedom. The control variables and testing procedure were the same as those used in the testing of the model free in pitch and plunge. Due to the absence of the plunge freedom, the risk of catastrophe was largely reduced. Excessive pitch angle was automatically limited by the aerodynamic nonlinearity.

Results and Discussion

The lift and moment coefficients of the aircraft model are shown in Fig. 5. The aerodynamic derivatives defined in the tunnel axis are given by the linear portion of the lift and moment curves. The results show the values of $C_{L\alpha} = 5.33$ and $C_{M\alpha} = -0.97$, which give the aircraft model an 18% static margin. Wing vibration frequencies were measured by ground vibration tests before the wind-tunnel tests. Table 2 gives the measured and calculated natural frequencies of the four graphite/epoxy wing components. For the $[15_2/0]_s$ and $[30_2/0]_s$ wings, the designations of first torsion and second bending are somewhat vague because of strong stiffness coupling.

Table 2 Natural frequencies of wings, Hz

	First bending		First torsion		Second bending	
Wing	Calc.	Exp.	Calc.	Exp.	Calc.	Exp.
$[0_2/90]_s$	11.1	11.4	36.2	37.6	69.3	71.8
$[15_2/0]_s$	8.4	9.0	46.7	45.3	58.7	64.3
$[30_2/0]_s$	5.6	5.8	40.5	37.4	60.6	58.4
$[-15_2/0]_s$	8.4	8.8	46.7	45.8	58.7	64.0

Cantilever Wing Divergence and Flutter

For comparison purposes, the linear and nonlinear flutter and divergence boundaries of the cantilever wing were tested and are presented in Fig. 6. Because of the flexibility of the wing model, aerodynamic nonlinearity, i.e., wing stall, would occur before the model was overstressed or failed. Aeroelastic instability was thus safely encountered and observed in the form of limit cycle oscillation. Linear aeroelastic phenomena, i.e., wing divergence and bending-torsion wing flutter, were interpreted at low fuselage (wing root) angles of attack.

The cantilever wing results shown in Fig. 6 are similar to those given earlier in Ref. 12. For the $[15_2/0]_s$ and $[30_2/0]_s$ wings, bending-torsion flutter occurred at low fuselage angles of attack. At higher angles, the bending-torsion flutter gradually changed to torsional stall flutter with an accompanying increase in the flutter frequency toward the single-mode torsional frequency and a decrease in the flutter speed. Calculations of the linear bending-torsion flutter speed given in Table 3 showed good agreement with experiment at low angles of attack. For the $[0_2/90]_s$ and $[-15_2/0]_s$ wings, divergence occurred at low fuselage angles of attack. This divergence condition was noted when the fuselage angle of attack could not be set small enough to keep the wing from "flipping over" to either one side or the other. At higher fuselage angles, the static divergence quickly changed to either a torsional stall flutter ($[0_2/90]_s$ wing) or a bending stall flutter ($[-15_2/0]_s$ wing), with an accompanying decrease in flutter speed. Calculations of the linear divergence speed given in Table 3 showed good agreement with experiment at low angles of attack.

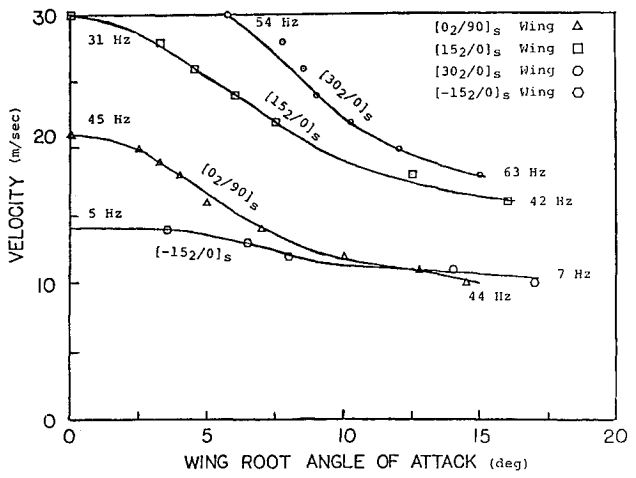

Fig. 6 Cantilever wing flutter and divergence boundaries.

Body Freedom Flutter and Support Instability

Body freedom flutter was predicted by the linear analysis and was observed in the wind-tunnel tests. There also existed, however, an additional tunnel support-related dynamic instability involving the model plunge and pitch motions. Before describing the body freedom flutter results, this tunnel support instability will first be discussed.

The original pitch support system involved no mechanical pitching stiffness except for a small amount of pendulum stiffness that gave it a 0.20 Hz pitching frequency in still air. Together with a 0.63 Hz plunging frequency resulting from the suspension spring, the analysis of a two-degrees-of-freedom tunnel-supported "rigid" model showed that a support instability would occur at 8 m/s and end at 31 m/s. The complete seven-mode aeroelastic analysis showed that wing flexibility could significantly modify the termination speed

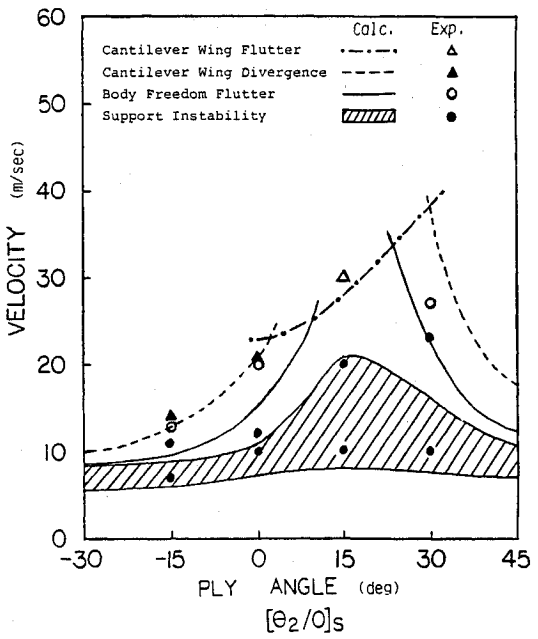

Fig. 7 Flutter and divergence boundaries for "free" model.

Table 3 Divergence, flutter, and support instability

Wing	$[0_2/90]_s$ Calc., m/s (Hz)	$[0_2/90]_s$ Exp., m/s (Hz)	$[15_2/0]_s$ Calc., m/s (Hz)	$[15_2/0]_s$ Exp., m/s (Hz)	$[30_2/0]_s$ Calc., m/s (Hz)	$[30_2/0]_s$ Exp., m/s (Hz)	$[-15_2/0]_s$ Calc., m/s (Hz)	$[-15_2/0]_s$ Exp., m/s (Hz)
Cantilever wing divergence	21	21	>60	—	45	—	13	14
Cantilever wing flutter	23 (23)	—	28 (30)	30 (31)	38 (33)	>30	>60	—
Model on support 1[a] support instability	8-11 (0.5-0.6)	10-12 (0.5-0.6)	8-21 (0.5-0.6)	10-20 (0.5-0.6)	8-16 (0.5-0.6)	10-23 (0.5-0.6)	6-9 (0.5-0.6)	7-11 (0.5-0.7)
Model on support 1 body freedom flutter	16 (2.1)	19 (2.7)	>60	>30	24 (2.1)	26 (1.7)	10 (1.3)	13 (2.1)
Body freedom flutter (free in pitch only)	13 (1.5)	17 (1.9)	>60	22 (1.4)	18 (1.4)	19 (1.2)	8 (0.9)	10 (1.0)
Model on support 2[b] body freedom flutter	16 (2.3)	20 (2.8)	>60	>30	23 (2.1)	27 (1.8)	10 (1.6)	13 (2.3)
"Free" model body freedom flutter	15 (2.0)	NA	>60	NA	22 (2.0)	NA	9 (1.2)	NA

[a]Support 1: original pitch frequency = 0.20 Hz. [b]Support 2: modified pitch frequency = 0.85 Hz.

of the support instability but not the onset speed. This was due to the small aeroelastic effect at the lower dynamic pressure and the significant effect at the higher dynamic pressures. The aeroelastic effect on the termination speeds was found to follow the tendency of the body freedom flutter, which became critical after the support stability was recovered. Figure 7 and Table 3 show the calculated and observed support instabilities and their good agreement for the four wings. Figure 8 shows an example of support instability where the model was seen to plunge unboundedly until it hit the top and bottom plunge stops. During the tests, the support instability appeared mild and could be flown through if the model was not given much of an initial disturbance.

The support instability arises from the interaction of the pitch and plunge modes of the "rigid" model. Since the pitch frequency increases with airspeed due to aerodynamic stiffening while the plunge frequency is independent of airspeed, there will be a frequency coalescence and mode transfer if the pitch frequency in still air is below the plunge frequency. Figure 9 illustrates the coalescing trends and mode transfer on an ω-V plot. To suppress this support instability, the original pitching frequency of 0.20 Hz was modified to 0.85 Hz by adding mechanical pitching springs so that now this frequency was above the plunge frequency of 0.63 Hz. This modified support system was tested and showed no signs of the support instability previously encountered. Figure 10 shows the frequency trend of the modified support system.

Body freedom flutter was observed during the tests wherever it was analytically predicted. Figure 11 shows an example of body freedom flutter for the $[0_2/90]_s$ wing. The wing bending was approximately in phase with the model pitch, while the plunge motion was about 180 deg out of phase, and the flutter mode exhibited a nodal point near the model nose position. The flutter frequency was at 2.8 Hz compared with the 11 Hz wing bending frequency and the 0.85 Hz model pitching frequency in still air. The body freedom flutter arises from the interaction of the aeroelastically destiffening wing mode with the aerodynamically stiffening rigid-body short period (pitch-plunge) mode. Figure 10 shows the coalescing trends of these modes on an ω-V plot for the $[0_2/90]_s$ wing, along with the major frequency components.

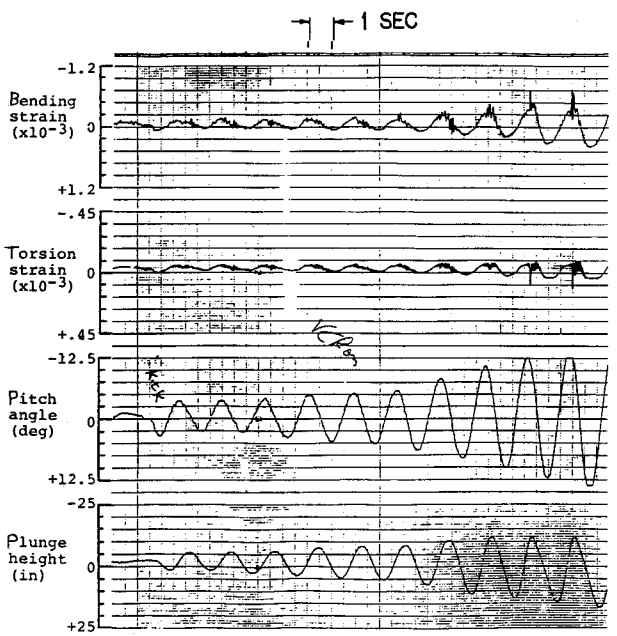

Fig. 8 Support instability, $[0_2/90]_s$ wing, $V = 10$m/s.

The body freedom flutter results of various wings tested are summarized in Table 3. Good agreement between calculated and observed instabilities was obtained for almost all cases. A typical calculated root locus plot using the seven-mode analysis is shown in Fig. 12. Also, it is seen from Table 3 that the presence of the support instability did not affect the body freedom flutter either analytically or experimentally. In Fig. 7, the predicted and measured body freedom flutter boundaries are compared with the cantilever wing divergence boundaries. The body freedom flutter is shown to be more critical than the wing divergence. The aircraft model with the $[15_2/0]_s$ wing demonstrated the best tailored aeroelastic behavior for all wings tested. Within the 30 m/s tunnel speed limit, no body freedom flutter was encountered. With the model steadily trimmed at a 2 deg pitch angle, bending-torsion wing flutter was observed at 29 m/s and became the critical instability mode as shown in Fig. 13.

Examination of the body freedom flutter boundary in Fig. 7 shows that the effect of aeroelastic tailoring follows the trend of cantilever wing divergence tailoring. This suggests that the wing destiffening is still the primary triggering mechanism of the body freedom flutter. The presence of rigid-body freedoms modifies the boundary conditions of the destiffened wing mode and ultimately changes the instability nature from static divergence to dynamic flutter.

The body freedom flutter results of the model free in pitch only are also compared with the other body freedom flutter results in Table 3. The absence of the plunging freedom resulted in a lower body freedom flutter speed, thereby giving a conservative flutter boundary.

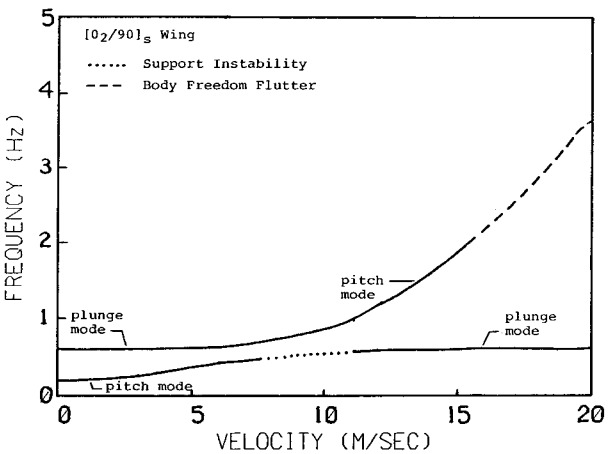

Fig. 9 ω-V plot, original support, $[0_2/90]_s$ wing.

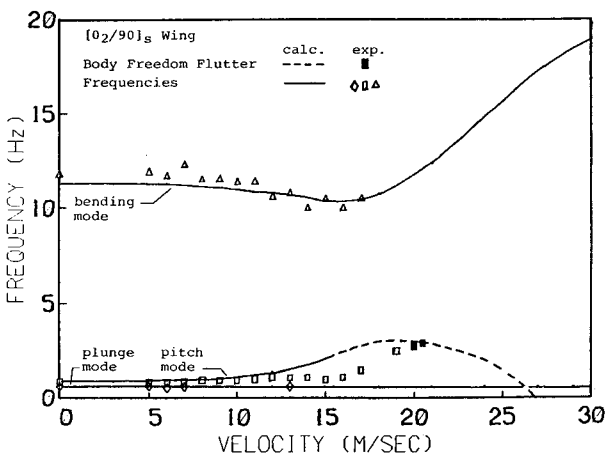

Fig. 10 ω-V plot, modified support, $[0_2/90]_s$ wing.

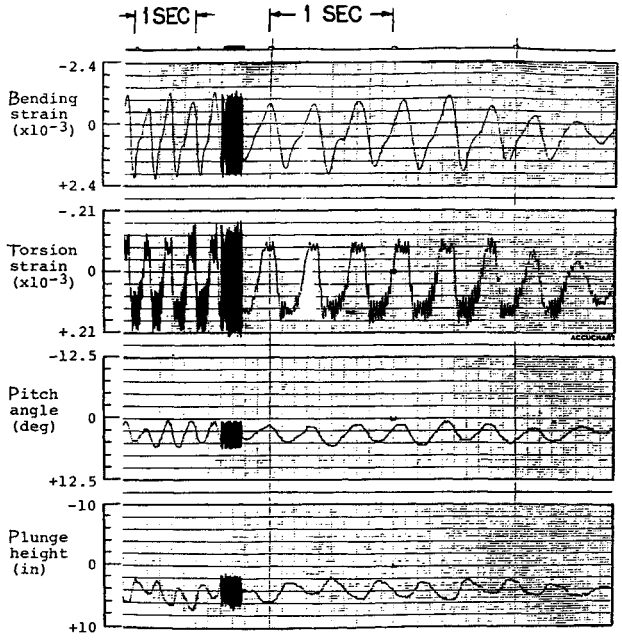

Fig. 11 Body freedom flutter, $[0_2/90]_s$ wing, $V=20$ m/s.

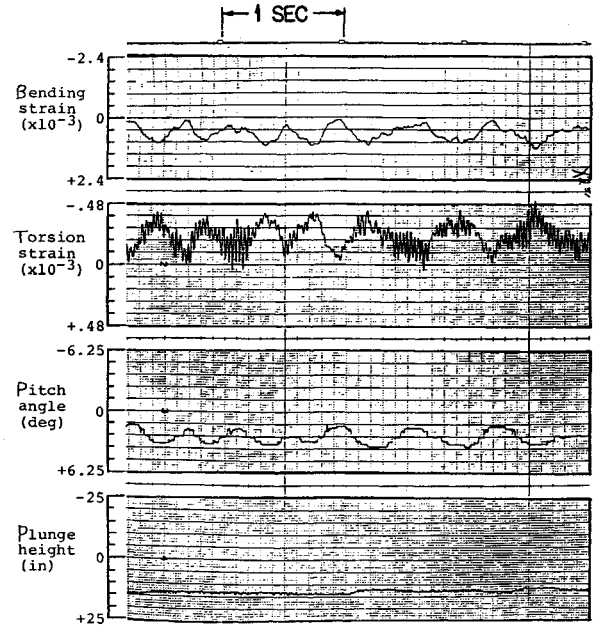

Fig. 13 Bending torsion flutter, $[15_2/0]_s$ wing, $V=29$ m/s.

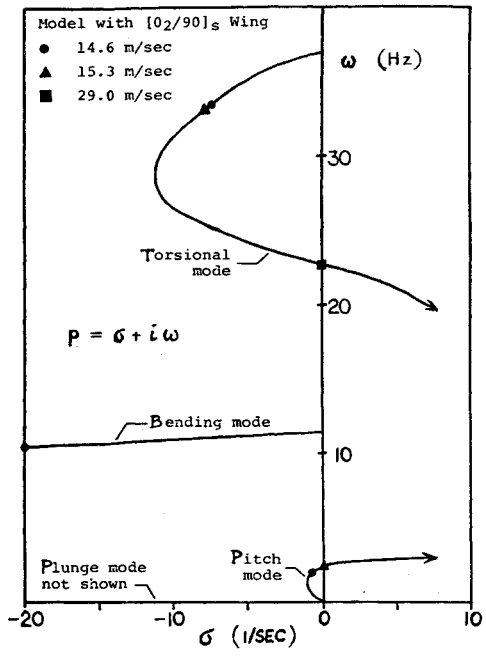

Fig. 12 Root locus stability plot, $[0_2/90]_s$ wing.

Conclusions

An analytical and experimental investigation was made of the aeroelastic flutter and divergence behavior of graphite/epoxy forward-swept wings with rigid-body pitch and plunge freedoms present. Experimental wind-tunnel data was obtained for a complete, two-sided 30 deg forward-swept wing aircraft model mounted with low friction bearings in a low-speed wind tunnel.

The tests revealed large variations in aeroelastic behavior for four different ply orientation wings. Body freedom flutter and bending-torsion flutter were observed, and regions of their occurrence were mapped.

The forward-swept wings developed body freedom flutter rather than divergence when rigid-body modes were present. This occurred at a lower speed than divergence but seemed to have the general trend of the divergence region.

A support-related dynamic instability involving the model's pitch and plunge motions was also encountered at low speeds. This instability could be eliminated by making the still-air model pitch frequency greater than the model plunge frequency, thereby avoiding a possible frequency coalescence at some airspeed.

For the model free in pitch only, body freedom flutter was again encountered, but at a lower airspeed. The presence of the plunge freedom apparently raises the flutter speed.

Tests conducted on the cantilever wings, i.e., with the aircraft model restrained in both plunge and pitch by the snubber cables, revealed the same aeroelastic behavior as noted earlier in Ref. 12. Linear divergence and bending-torsion flutter occurred at low angles of attack and nonlinear torsional stall flutter and bending stall flutter occurred at the higher angles. The static divergence condition changed to either a torsional or bending stall at moderate angles of attack.

Linear theory at low angles of attack provided good agreement with the observed bending-torsion flutter, body freedom flutter, support instability, and divergence phenomena. At higher angles of attack, there was a transition to nonlinear torsional stall flutter and bending stall flutter limit cycles, which are not as well understood.

The present investigation extends the experimental base for aeroelastic tailoring with composites and, along with the corresponding theoretical analyses, may provide some insight into the actual aeroelastic behavior of forward-swept composite wing aircraft in free flight. Further details, trends, and specific cases for this investigation can be found in Ref. 14.

Acknowledgments

The authors wish to acknowledge the assistance of Karen Needels in the experiments and data reduction. They also wish to acknowledge the support of the U.S. Air Force Office of Scientific Research under Contract AFOSR F49620-85-C-0099, Dr. Anthony Amos, technical monitor.

References

[1]Shirk, M.H., Hertz, T.J., and Weisshaar, T.J., "Aeroelastic Tailoring—Theory, Practice, and Promise," *Journal of Aircraft*, Vol. 23, Jan. 1986, pp. 6-18.

[2]Krone, N.J., "Divergence Elimination with Advanced Composites," AIAA Paper 75-1009, 1975.

[3]Weisshaar, T.A., "Aeroelastic Tailoring of Forward Swept Composite Wings," *Journal of Aircraft,* Vol. 18, Aug. 1981, pp. 669-676.

[4]Sherrer, V.C., Hertz, T.J., and Shirk, M.H., "Wind Tunnel Demonstration of Aeroelastic Tailoring Applied to Forward Swept Wings," *Journal of Aircraft,* Vol. 18, Nov. 1981, pp. 976-983.

[5]Hertz, T.J., Shirk, M.H., Ricketts, R.H., and Weisshaar, T.A., "On the Track of Practical Forward Swept Wings," *Aeronautics and Astronautics,* Vol. 20, Jan. 1982, pp. 40-53.

[6]Weisshaar, T.A., Zeiler, T.A., Hertz, T.J., and Shirk, M.J., "Flutter of Forward Swept Wings, Analyses and Tests," AIAA Paper 82-0646, May 1982.

[7]Miller, G.D., Wykes, J.H., and Brosnan, M.J., "Rigid Body—Structural Coupling on a Forward Swept Wing Aircraft," *Journal of Aircraft,* Vol. 20, Aug. 1983, pp. 696-702.

[8]Weisshaar, T.A. and Foist, B.L., "Vibration and Flutter of Advanced Composite Lifting Surfaces," AIAA Paper 83-0961, May 1983.

[9]Noll, T.E., Eastep, F.E., and Calico, R.A., "Active Suppression of Aeroelastic Instabilities on a Forward Swept Wing," *Journal of Aircraft,* Vol. 21, March 1984, pp. 202-208.

[10]Chipman, R., Rauch, F., Rimer, M., Muniz, B., and Ricketts, R.H., "Transonic Tests of a Forward Swept Wing Configuration Exhibiting Body Freedom Flutter," AIAA Paper 85-0689, April 1985.

[11]Hollowell, S.J. and Dugundji, J., "Aeroelastic Flutter and Divergence of Stiffness Coupled, Graphite/Epoxy Cantilevered Plates," *Journal of Aircraft,* Vol. 21, Jan. 1984, pp. 69-76.

[12]Landsberger, B. and Dugundji, J., "Experimental Aeroelastic Behavior of Unswept and Forward Swept Graphite/Epoxy Wings," *Journal of Aircraft,* Vol. 22, Aug. 1985, pp. 679-686.

[13]Kinnaman, E.B., "Flutter Analysis of Complex Airplanes by Experimental Methods," *Journal of the Aeronautic Sciences,* Vol. 19, Sept. 1952, pp. 577-584.

[14]Chen, G.S., "Aeroelastic Behavior of Forward Swept Graphite/Epoxy Wing Aircraft with Rigid Body Freedoms," Sc.D. Thesis, Dept. of Aeronautics and Astronautics, Massachusetts Institute of Technology, Cambridge, May 1986 (Also TELAC Rept. 86-14, MIT, May 1986).